Published in final edited form as:
Arterioscler Thromb Vasc Biol. 2023 September ; 43(9): e358–e372. doi:10.1161/ATVBAHA.123.319122.

Effects of age, sex, and extracellular matrix integrity on aortic dilatation and rupture in a mouse model of Marfan syndrome

Dar Weiss,
Department of Biomedical Engineering, Yale University, New Haven, CT

Bruno V. Rego,
Department of Biomedical Engineering, Yale University, New Haven, CT

Cristina Cavinato,
Department of Biomedical Engineering, Yale University, New Haven, CT

David S. Li,
Department of Biomedical Engineering, Yale University, New Haven, CT

Yuki Kawamura,
Department of Biomedical Engineering, Yale University, New Haven, CT

Nir Emuna,
Department of Biomedical Engineering, Yale University, New Haven, CT

Jay D. Humphrey
Department of Biomedical Engineering, Yale University, New Haven, CT

Vascular Biology and Therapeutics Program, Yale School of Medicine, New Haven, CT

Abstract

BACKGROUND: Transmural failure of the aorta is responsible for substantial morbidity and mortality; it occurs when mechanical stress exceeds strength. The aortic root and ascending aorta are susceptible to dissection and rupture in Marfan syndrome, a connective tissue disorder characterized by a progressive reduction in elastic fiber integrity. Whereas competent elastic fibers endow the aorta with compliance and resilience, cross-linked collagen fibers confer stiffness and strength. We hypothesized that postnatal reductions in matrix crosslinking increase aortopathy when turnover rates are high.

METHODS: We combined *ex vivo* biaxial mechanical testing with multimodality histological examinations to quantify expected age- and sex-dependent structural vulnerability of the ascending aorta in *Fbn1*$^{C1041G/+}$ Marfan vs. wild-type mice without and with 4-week exposures to β-aminopropionitrile (BAPN), an inhibitor of lysyl oxidase mediated crosslinking of newly synthesized elastic and collagen fibers.

Address for Correspondence: Dar Weiss, Ph.D., Department of Biomedical Engineering, Yale University, New Haven, CT 06520 USA, dar.weiss@yale.edu, +1-203-508-2118.

Disclosures
The authors declare no conflicts of interest.

RESULTS: We found a strong BAPN-associated sexual dimorphism in aortic dilatation in Marfan mice and aortic rupture in wild-type mice, with dilatation correlating with compromised elastic fiber integrity and rupture correlating with compromised collagen fibril organization. A lower incidence of rupture of BAPN-exposed Marfan aortas associated with increased lysyl oxidase, suggesting a compensatory remodeling of collagen that slows disease progression in the otherwise compromised *Fbn1*$^{C1041G/+}$ aorta.

CONCLUSIONS: Collagen fiber structure and function in the Marfan aorta is augmented, in part, by increased lysyl oxidase in female and especially male mice, which improves structural integrity, particularly via fibrils in the adventitia. Preserving or promoting collagen crosslinking may represent a therapeutic target for an otherwise vulnerable aorta.

Graphical Abstract:

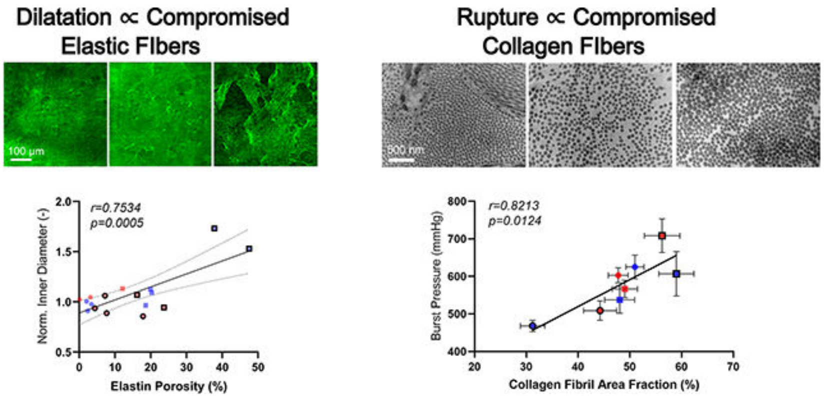

Keywords

fibrillin-1; collagen; lysyl oxidase; β-aminopropionitrile (BAPN); male; female; aneurysm

INTRODUCTION

Marfan syndrome (MFS) results from mutations in the gene (*FBN1*) that codes fibrillin-1[1], an elastin-associated glycoprotein important in extracellular matrix development and homeostasis[2]. Premature mortality in MFS results from rupture of the thoracic aorta, often secondary to aneurysm. Much has been learned clinically, but mouse models provide additional insight. Two common mouse models are *Fbn1*$^{mgR/mgR}$, which are hypomorphic for wild-type fibrillin-1[3], and *Fbn1*$^{C1041G/+}$ (*aka Fbn1*$^{C1039G/+}$), which express mutant fibrillin-1[4]. Both models exhibit abnormal histological features in the thoracic aorta, with aneurysm[5,6]. The dilated MFS aorta is characterized mechanically by decreased resilience, consistent with compromised elastic fiber integrity, and increased stiffness, consistent with altered mechano-regulation of collagen fibers by intramural cells[7,8].

Notwithstanding ubiquitous fragmentation and degradation of elastic lamellae in the aorta of MFS patients and mice, which has been suggested to drive dilatation, rupture of the aorta stems largely from compromised collagen fibers, which normally endow the wall with stiffness and strength.[9,10] RNA sequencing reveals increased transcripts for fibrillar collagens in MFS in humans and both common mouse models[11,12] consistent with histological evidence of increased collagen. Compromised elastic fibers also affect macroscale collagen properties, including fiber undulation and stiffness[13]. Thus, although the monogenic mutation in MFS directly affects elastic fibers, there appears to be important effects on collagen organization, accumulation, and integrity, which requires appropriate cross-linking to yield mechanically competent fibers. There is a need to better assess roles that collagen play in the MFS aorta.

Lysyl oxidase (LOX) initiates covalent cross-linking of newly synthesized elastic and collagen fibers, hence contributing to their biomechanical properties[14,15]. A recent study suggested that enhanced LOX-mediated collagen accumulation helps to protect against aortic dilatation ($Fbn1^{C1041G/+}$) and rupture ($Fbn1^{mgR/mgR}$)[16]. There was, however, no detailed assessment of the biomechanical phenotype. Cell biological and standard histological findings are revealing, but there is a need for direct functional readouts of the mechanical state of the aorta because mechanical failure – dissection and rupture – is ultimately responsible for the morbidity and mortality. A goal of this work was to test the hypothesis that postnatal reductions in collagen crosslinking compromise aortic properties and increase aortopathy. Toward this end, we quantified and compared histo-mechanical effects of inhibiting LOX with β-aminopropionitrile (BAPN) as a function of age (young, older), sex (female, male), and genotype (wild-type, MFS), seeking insight into possible benefits of preserving or promoting collagen crosslinking in a structurally vulnerable aorta.

METHODS

Data Availability

Quantification of primary matrix constituents from stained-histological sections is in Tables S1, S2, and key biomechanical findings are given numerically in Tables S3, S4. Additional data that support our findings are available from the corresponding author upon reasonable request.

Animals

All live animal research was approved by the Institutional Animal Care and Use Committee of Yale University. Mice were generated by breeding $Fbn1^{+/+}$ females and $Fbn1^{C1041G/+}$ males (Jackson Laboratories). Littermate $Fbn1^{+/+}$ (wild-type, WT) and $Fbn1^{C1041G/+}$ (Marfan syndrome, MFS) mice were maintained on normal chow and water until death, either natural or scheduled euthanasia. To prevent cross-linking of newly synthesized elastic or collagen fibers, female and male WT (FWT, MWT) and MFS (FMFS, MMFS) mice were given BAPN (Sigma Aldrich) *ad libitum* in the drinking water (2 g/l) for 4 weeks[17] beginning at either 4 or 8 weeks of age. These ages were chosen because elastic lamellae appear to be biomechanically mature by ~4 weeks whereas collagen organization does not reach steady state until ~8 weeks, when the aorta is biomechanically mature[18].

Of the 357 mice used, those given BAPN were selected randomly based solely on availability of an appropriate age (4 vs. 8 weeks), sex (F vs. M), and genotype (WT vs. MFS) at the time of each pre-scheduled study; that is, consistent with ARRIVE guidelines (Supplementary Materials), there was no selection bias. Given the expected higher mortality when giving BAPN from 4–8 weeks of age, 74 WT (39 F and 35 M) and 87 MFS (45 F and 42 M) mice were used to construct Kaplan-Meier survival curves. Following euthanasia (CO_2 inhalation) of mice surviving a 4-week study period, the ascending aorta was excised for detailed examination at either 8 or 12 weeks of age, without or with 4 weeks of BAPN, thus resulting in 16 primary groups. Standard tail-cuff blood pressures were collected prior to euthanasia.

Mechanical Testing

Expecting both MFS and BAPN to alter the extracellular matrix, we used custom biaxial mechanical testing to quantify passive aortic behaviors. Supplemental Figure S1 shows the sequence of histo-mechanical tests, which were necessarily limited to mice that survived a scheduled 4-week study. We used two custom *ex vivo* testing devices to independently quantify bulk[19] and regional[20,21] mechanical behaviors in the primary material directions, circumferential and axial. First, for bulk testing, aortic segments were cannulated with custom glass micro-pipets through the aortic valve (proximal end) and brachiocephalic artery (distal end), secured with 6-O sutures, and placed within a computer-controlled testing device in a Hank's buffered salt solution (HBSS) at room temperature to ensure passive responses. The computer preconditioned the specimens cyclically from 10 to 120 mmHg while maintaining fixed the energetically preferred (*in vivo*) axial stretch, λ_z^{iv}, then subjected the specimens to a sequence of 7 protocols: cyclic pressurization from 10 to 140 mmHg at 3 fixed axial stretches (λ_z^{iv} and ±5% of this value) and cyclic axial loading from 0 to f_{max} at 4 fixed luminal pressures (10, 60, 100, 140 mmHg), where f_{max} (in mN) was the specimen-specific value at 140 mmHg and $1.05\lambda_z^{iv}$. Four channels of data (outer diameter, distending pressure, axial length, and axial force) were recorded on-line. With over 100 data points collected per channel over seven protocols, the computer collected over 2800 data points per sample per loading cycle (yielding >2800×80 = 224000 data points for comparison across 16 groups, or >14000 data points per group). Computer control using high resolution actuators yields data with smaller standard deviations (SD) than when collected with commercially available devices[19].

Second, panoramic digital image correlation (pDIC) was used to quantify regional mechanical behaviors for a sub-set of specimens selected randomly from approximately half of the 8-week old mice, which were expected to exhibit more severe phenotypes than 12-week old mice. Briefly[20], the outer surface of the adventitia was stained with Evans blue dye, then air-brushed with white India ink to form a speckle pattern (Figure S2). Each specimen, re-cannulated on a custom co-axial triple-needle assembly, was placed within a custom 45-degree-angle conical mirror, submerged in HBSS at room temperature, and connected to a pressure-controlled line. Images containing both the reflected speckle pattern and a static calibration target were captured from 8 rotationally symmetric views by a vertically located digital camera (DALSA Falcon 4M30) at 42 quasi-static configurations: 14 pressures (10–140 mmHg, in 10 mmHg increments) and 3 axial stretches (λ_z^{iv} and ±5% of this value) for a total of 42×8 = 336 images per specimen. A reference configuration was defined at 80 mmHg and *in vivo* axial stretch. Custom MATLAB scripts unwrapped the pDIC images, and normalized cross-correlations related pairs of images over all deformed configurations. A ray-tracing procedure enabled reconstruction of the physical location of each correlated point over the surface, thus allowing straightforward computation of full-field surface deformations. Local optical coherence tomography (OCT)-derived thicknesses collected at 100 cross-sections along the length of the vessel were mapped onto the pDIC-reconstructed geometry using an automatic co-registration pipeline[22]. Detailed information about our multimodality pDIC and OCT pipeline can be found elsewhere[20,21,23], noting that collecting over 1000 data points at 42 mechanical states yields >42000 data points per sample. Hence, the pDIC comparisons were based on over 42000×23 = 966000 data points, again exploiting the strategy of increasing the data collected per sample while reducing variability by using highly protocolized, high resolution methods. Finally, in a randomly selected sub-set of mice (Figure S1), vessels were then placed within a simple experimental system and pressurized at their *in vivo* axial length until failure to determine the burst pressure.

Material Characterization

Expecting both MFS and BAPN to adversely affect material stiffness and elastic stored energy, we used an independently validated[24] four-fiber family constitutive relation to describe the passive biaxial mechanical behavior of the ascending aorta[7,25]. First, the unloading portion of the last cycle of all 7 pressure-diameter and axial force-length tests were fit simultaneously using a Levenberg-Marquardt nonlinear regression, with multiple (typically 5) initial guesses used to determine global minima. Using data from unloading reveals the bulk elastic energy stored during deformation that would be available to work on the distending fluid. This four-fiber family model is written in terms of a stored energy function W,

$$W\left(\mathbf{C},\mathbf{M}^i\right)=\frac{c}{2}\left(I_{\mathrm{C}}-3\right)+\sum_{i=1}^{4}\frac{c_1^i}{4c_2^i}\left\{\exp\left[c_2^i\left(IV_{\mathrm{C}}^i-1\right)^2\right]-1\right\},$$

where the 8 parameters to be determined via regression are c (kPa), c_1^i (kPa), c_2^i (−), and $\alpha_0^{3,4}$ (radians), with $i = 1,2,3,4$ denoting predominant fiber family directions: axial ($\alpha_0^1 = 0$), circumferential ($\alpha_0^2 = \pi/2$), and two symmetric diagonal $(\alpha_0^{3,4} = \pm\alpha_0)$. $I_{\mathrm{C}} = tr(\mathbf{C})$ and $IV_{\mathrm{C}}^i = \mathbf{M}^i \cdot \mathbf{CM}^i$ are coordinate invariant measures of finite deformation, with $\mathbf{C} = \mathbf{F}^{\mathrm{T}}\mathbf{F}$ computed from the experimentally measured deformation gradient $\mathbf{F} = \mathrm{diag}[\lambda_r, \lambda_\theta, \lambda_z]$, with $det\mathbf{F} = 1$ for incompressibility. The direction of the i^{th} family of fibers was $\mathbf{M}^i = [0,\ \sin\alpha_0^i,\ \cos\alpha_0^i]$, with α_0^i denoting a fiber angle relative to the axial direction in the reference configuration. Values of mean biaxial wall stress and material stiffness were computed from the stored energy function and calculated at a common pressure of 100 mmHg.

Second, pDIC data were used to estimate best-fit parameters of our four-fiber constitutive relation locally, at ~1000 sites around the circumference and along the length of each specimen: 40 circumferential patches defined by $\Theta_m,\ m \in [1,40]$ × 25 axial patches defined by $Z_n,\ n \in [1,25]$, with $\Theta \in [-\pi, \pi]$ and $Z \in [0, L]$, where L is the length of the specimen in the *in vivo* relevant reference configuration. Green strains ($\mathbf{E} = (\mathbf{C} - \mathbf{I})/2$, where $\mathbf{I}$ is the second-order identity tensor) were calculated at each Gauss point of a 4-noded rectangular surface patch using the open-source finite element software, FEBio while assuming an incompressible neoHookean strain energy function. Then, the material behavior at each Gauss point was modeled with the aforementioned four-fiber family W. The principle of virtual power was enforced at each Gauss point to achieve inverse characterization within each $\Theta_m Z_n$ element[22]. Once completed, the final set of identified parameters at each element was used to compute full-field distributions of the different mechanical metrics, as described previously[21,22,26].

To perform spatially local statistical analyses of group-wise differences in geometric and mechanical properties, we developed an automatic pipeline to parametrize and co-register all pDIC+OCT-derived data. Starting from each vessel-specific quadrilateral patch obtained from pDIC, we performed a principal component analysis of nodal coordinates and automatically identified two objective landmarks on the vessel (Figure S3): the outermost point on the outer curvature and point of ligation on the distal end. To control for differences in vessel length, we linearly transformed the length scale along the axial direction such that a corresponding size-independent "axial coordinate" had a value of 0 at the outermost point on the outer curvature and a value of 1 at the distal ligature. Because the vessel geometry goes past these locations, resulting axial coordinate values extend beyond the [0, 1] interval. We then parametrized the vessel circumferentially over [−1, 1] using the in-plane angle of each patch node with respect to the local centerline, with periodicity at −1 and 1 (the middle of the outer curvature). For co-registration and analysis, we re-discretized the surface within the correspondent region along the axial direction that was shared by all vessels. Within this region, the vessel surface was segmented into anatomically relevant regions, namely, "proximal" and "distal" along the axial direction and "inner," "dorsal," "outer," and "ventral" around the circumference (Figure S3).

At each mesh point within the correspondent region of the wall, we quantified effects of age, sex, genotype, and BAPN on local luminal radius and wall thickness. Denoting a metric of interest as y, we modeled group- and location-specific log-values as a linear function of the predictors using

$$\ln(y) = \beta_0 + \beta_{\mathrm{Sex}}\mathbf{1}_{\mathrm{Female}} + \beta_{\mathrm{MFS}}\mathbf{1}_{\mathrm{MFS}\,\wedge\,\neg\mathrm{BAPN}} + \beta_{\mathrm{BAPN}}\mathbf{1}_{\neg\mathrm{MFS}\,\wedge\,\mathrm{BAPN}} + \beta_{\mathrm{MFS-BAPN}}\mathbf{1}_{\mathrm{MFS}\,\wedge\,\mathrm{BAPN}},$$

where $\mathbf{1}$ is the indicator function for the subscripted condition(s), "$\wedge$" denotes the logic AND function, and "$\neg$" denotes the logic NOT function. Best-fit parameters β_i were estimated via least-squares regression of $\ln(y)$. Exponentiating both sides,

$$\begin{aligned} y = {} & \exp(\beta_0) \times \exp(\beta_{\mathrm{Sex}}\mathbf{1}_{\mathrm{Female}}) \times \exp(\beta_{\mathrm{MFS}}\mathbf{1}_{\mathrm{MFS}\,\wedge\,\neg\mathrm{BAPN}}) \times \exp(\beta_{\mathrm{BAPN}}\mathbf{1}_{\neg\mathrm{MFS}\,\wedge\,\mathrm{BAPN}}) \\ & \times \exp(\beta_{\mathrm{MFS-BAPN}}\mathbf{1}_{\mathrm{MFS}\,\wedge\,\mathrm{BAPN}}), \end{aligned}$$

where the baseline $\exp(\beta_0)$ corresponds to the predicted value for non-BAPN MWT mice, $\exp(\beta_{\mathrm{Sex}})$ is the fold-change when female (within any group), $\exp(\beta_{\mathrm{MFS}})$ is the fold-change for MFS without BAPN, $\exp(\beta_{\mathrm{BAPN}})$ is the fold-change for BAPN without MFS, and $\exp(\beta_{\mathrm{MFS-BAPN}})$ is the fold-change for MFS with BAPN. These fold changes are visualized as spatial maps.

Multiphoton microscopy

We expected BAPN to differentially affect elastic and collagen fiber organization. Hence, in a subset of mice ($n = 4 – 5$ selected randomly per group at 8 weeks of age; see Figure S1), and following standard mechanical testing, vessels were held at 80 mmHg and the specimen specific axial stretch while immersed in HBSS at room temperature. A LaVision Biotec TriMScope two-photon microscope operated with a TiSa laser tuned at 820 nm was used with an Olympus 20X objective lens (N.A. 0.95). Three signals were: second harmonic generation for fibrillar collagen (390–425 nm), two-photon excited fluorescence for elastin (500–550 nm), and SYTO17 red fluorescence of cell nuclei (above 550 nm). Three-dimensional images were acquired at a consistent location corresponding to the center of the outer curvature, with a numerical imaging resolution of 0.48 μm/pixel and out-of-plane (radial axis) step size of 1 μm/pixel. All images were processed as previously described[5]. Briefly, layer-specific cell densities were calculated as the number of cells per unit volume by counting nuclei within defined sub-volume and normalizing by the appropriate layer-specific thickness. Three cell groups were considered based on characteristic shapes of their nuclei and radial location: endothelial (monolayer on intima), smooth muscle (within the media), and cells within the adventitia. A three-dimensional elastin porosity was defined as the ratio of the volume identified as voids and the volume occupied by elastic fibers, including lamellar and intra-lamellar. For this purpose, an adaptive 3D filter was applied to the remaining volume to reduce possible inhomogeneities due to local waviness of the elastic lamellae, the image was binarized using the automatic local Phansalkar thresholding method, and the volume of the identified voids was quantified as a black-to-white ratio. Description of collagen fiber bundles focused on in-plane (axial-circumferential) parameters of fiber straightness and bundle width. Straightness was computed as the ratio of end-to-end to total fiber length; bundle width was measured as the transversal section of multiple bundles[5,21].

In comparison to standard histological sections, multiphoton microscopy allows quantification over a broader spatial domain (500 μm × 500 μm x full wall thickness), thus yielding more robust averages over larger numbers of cells, fibers, and lamellar structures. Nevertheless, these data were assessed qualitatively, not statistically, given the small number of samples per sex and the sexually dimorphic findings that emerged from the standard biaxial testing. These data are included in Supplemental Material because they support the histological findings using an independent method.

Histology

Following the multi-step mechanical testing, vessels were prepared for standard immuno-histological examination or electron microscopy. For the former, we evaluated standard histological features consistent with most reports on the *Fbn1*$^{C1041G/+}$ aorta. Segments were fixed overnight in a 10% neutral buffered formalin solution and stored in 70% ethanol at 4°C until embedding in paraffin and serial sectioning at 5 μm. Mounted slides were stained with either picro-sirius red (PSR), to detect fibrillar collagens in a spectrum from red-to-green, or Movat’s pentachrome (MOV), to detect elastin in black, collagen in yellow/brown, cytoplasm in red/purple, mucoid material (glycosaminoglycans) in aqua/blue, and fibrin in pink/red.(Figure S4). Additional sections were immuno-stained with a primary antibody (ab174316 Abcam) to detect lysyl oxidase in brown. Images were acquired using an Olympus BX/51 microscope at 20X magnification: MOV and IHC as standard bright-field images and PSR as dark-field images using polarized light, with separate exposures to capture medial and adventitial collagens[5]. MOV sections were used to compute medial and adventitial wall areas as well as areas for elastin, cytoplasm, collagen, glycosaminoglycans, and fibrin. PSR images were used to categorize collagen fibers as thick (red/orange) or thin (yellow-green) in medial exposure images.

Transmission Electron Microscopy

Expecting BAPN to induce changes in collagen at the fibril level, other aortic segments were fixed in 2.5% glutaraldehyde/2% paraformaldehyde in sodium cacodylate buffer for 2 h at 4°C. Samples were then rinsed in sodium cadodylate buffer before post-fixation in 1% osmium tetraoxide for 1 h and subsequent staining using 2% uranyl acetate for 1 h. Samples were washed and embedded in resin and viewed using a FEI Technai Biotwin electron microscope[27]. To analyze spatial distributions, sizes, and shapes of collagen fibrils, we used a novel semi-automated pipeline to segment individual fibrils. Briefly[28], the user initially selects regions to exclude from the analysis—for example, perivascular tissue rather than adventitial collagen fibrils (Figure S5). The image is then smoothed using a Gaussian filter with bandwidth equal to 0.3% of the smallest dimension (height or width) of the image. To binarize the filtered image into fibril and non-fibril pixels, a bivariate quadratic function $f_1(u, v)$ is first fit to the intensity values $I_{\text{filt}}(u, v)$ using a least-squares regression with a Cauchy weight function, where (u, v) are pixel coordinates. The modeled intensity values $f_1(u, v)$ are adopted as a local adjustment factor, and the intensity values of the filtered image are adjusted using

$$I_{\text{adj}}(u, v) = \left(I_{\text{filt}}(u, v)\right)^{\ln(0.5)/\ln(f_1(u, v))},$$

such that pixels with intensity $I_{\text{filt}}(u, v) = f_1(u, v)$ are mapped to 0.5. This spatially heterogeneous (yet smooth) adjustment attenuates the influence of regional variations in image intensity (e.g., due to non-uniform lighting) during the binarization step. Using Otsu's method[29], the transformed image is then binarized (I_{bin}) according to an optimal threshold, with dark pixels categorized as fibrils.

For each pixel in I_{bin}, the Euclidean distance to the nearest non-fibrillar pixel is computed to produce a distance field D with the same dimensions as I_{bin}. Then, for different Gaussian filter bandwidths σ_i (from 0.5 to 10 pixels, in steps of 0.5 pixels), the number of local peaks $N(\sigma_i)$ in $D_{\text{filt}}(\sigma_i)$—taken to be the number of "detected" fibrils—is computed. A 5th-degree polynomial $p(\sigma)$ is fit to the resulting data $(\sigma_i,\ N(\sigma_i))$, from which the optimal bandwidth σ^* is considered to be the lowest positive σ where $(dp/d\sigma)^2$ reaches a local minimum. Although $p(\sigma)$ is generally monotonically decreasing within the interval of interest, σ^* corresponds to the lowest positive σ where the slope of $p(\sigma)$ is locally the nearest to 0, meaning that the number of detected fibrils is minimally sensitive to filter bandwidth. The first estimate of the fibrils' centroid is given by local peaks in $D_{\text{filt}}(\sigma^*)$, with corresponding Voronoi cells defining a first estimate of fibril "neighborhoods" (Figure S5). Newly segmented fibril pixels are then clustered by fitting a 2D Gaussian mixture model to the fibril pixel coordinates, using the current centroid locations as an initial guess for the N cluster means and Voronoi cell memberships as initial cluster assignments. After fitting the model, posterior membership probability fields $P_i(u, v)$ are computed over the entire image for each cluster i (i.e., each fibril), and fibril neighborhood boundaries are redefined as $P_i(u, v) = 0.5$. The cross-sectional area of each fibril is computed by summing areas of all fibrillar pixels within the neighborhood boundary. At the group level, distributions of fibril area are computed via a kernel density estimation of log-transformed areas to enforce strictly positive support. Under the approximation that fibril pixel coordinates belonging to a particular fibril are uniformly distributed within an ellipse, major and minor radii are $r_{\text{major}} = 2\sqrt{\alpha_{\text{max}}}$ and $r_{\text{minor}} = 2\sqrt{\alpha_{\text{min}}}$, where α_{max} and α_{min} are maximum and minimum eigenvalues of the covariance matrix for those pixel coordinates.

Statistics

Due to deviations from normality (data that failed to pass Kolmogorov-Smirnov normality test), we used the nonparametric Kruskal Wallis one-way ANOVA on Ranks followed by Dunn’s post-hoc test for multiple comparisons to interpret geometric and mechanical metrics across the 16 study groups. Many of the key metrics derive from nonlinear parameter estimation (Levenberg-Marquardt or derivative-free genetic algorithms) of large data sets (>2800 or 42000 data points per specimen, respectively). Increasing the data collected per specimen and reducing experimental errors via computer control increases rigor and reproducibility, thus enabling statistically significant findings to be achieved with fewer specimens per group (e.g., $n = 5$ per biomechanical group), as confirmed using nonparametric bootstrapping[19]. Correlations, where appropriate, were assessed using the nonparametric Spearman’s rank correlation coefficient, r The Kaplan-Meier product limit estimator was used to analyze survival distributions and its statistics were analyzed using log-rank test. For all reported comparisons, a value of $p < 0.05$ was considered significant. Multiple levels of statistically significant differences across groups are indicated in each figure, as appropriate.

RESULTS

BAPN Differentially Affects Microstructural Composition

Transverse cross-sections of the ascending aorta ($n = 5 - 9$ for each of the 16 groups; Figure S1) stained with Movat’s pentachrome revealed age-, sex-, and genotype-dependent differences in medial and adventitial composition due to BAPN (Figures 1, S6; Tables S1, S2). Changes were more dramatic in mice given BAPN from 4–8 weeks of age than when given from 8–12 weeks of age. Similarly, changes tended to be greater in male than in female mice, with the greatest change in composition being in the younger male MFS aortas. BAPN-induced thickening of these MFS aortas arose mainly from increases in adventitial collagens as well as medial, and to a lesser extent adventitial, glycosaminoglycans, without any grossly adverse effects of BAPN on the elastic lamellae. The increases in adventitial thickness were accompanied by increases in adventitial cell density, which contrasted with decreases in medial smooth muscle cell and luminal cell densities based on cytoplasmic staining.

BAPN Differentially Affects Aortic Geometry, Elasticity, and Stiffness

Changes in microstructure are expected to translate into tissue-level changes in geometric and mechanical properties. Pressure-diameter behaviors ($n = 5$ per group; Figure S1) were quantified *ex vivo* under physiological levels of biaxial loading (Figure 2); they were similar across the 4 baseline groups (MWT, FWT, MMFS, FMFS) when evaluated at both 8 (4–8 week groups) and 12 (8–12 week groups) weeks of age, consistent with the mild early phenotype of the $Fbn1^{C1041G/+}$ aorta. By contrast, mice given BAPN from 4–8 weeks showed marked changes, including dilatation of MFS aortas, especially in males. Mice given BAPN from 8–12 weeks showed similar, though attenuated, behaviors. Coupled with associated changes in stress-stretch behaviors (Figure S7), these results revealed functional consequences of the aforementioned age- and sex-dependent differences in wall composition between WT and MFS aortas when LOX was blocked with BAPN early (4–8 weeks) versus later (8–12 weeks).

Comprehensive biomechanical phenotyping requires examination of additional geometric (inner radius, wall thickness, and *in vivo* axial stretch) and biaxial (circumferential and axial) mechanical metrics (including elastic energy storage and material stiffness) under physiological loading (Figures 3, S8; Tables S3, S4). Again with $n = 5$ per group (Figure S1), wall thickness changed less than 3% in male and female WT aortas when BAPN was given from 4–8 weeks but decreased ~15% when given from 8–12 weeks. By contrast, loaded wall thickness increased dramatically in MFS aortas, especially when BAPN was started early (~3-fold in males, ~1.9-fold in females) but also later (41% and 28% increases, respectively). BAPN only blocks cross-linking of newly deposited elastic and collagen fibers, with the former expected to affect elastic energy storage and the latter material stiffness. Giving BAPN from 4–8 weeks reduced energy storage in WT (25% in males, 32% in females) and especially MFS (66% in males, 62% in females) aortas; reductions were less when BAPN was given from 8–12 weeks in both WT (<10% in both sexes) and MFS (22% in males, 27% in females) aortas, noting that energy storage is naturally lower in MFS at 12 weeks (Figures 3B, S8B). These trends were paralleled by reductions in *in vivo* values of axial stretch (Figures 3F, S8F), both when BAPN was started early (<6% reductions in male and female WT, 19% and 18% MFS) and later (<5% in male and female WT, 5–10% in MFS). Results for circumferential material stiffness were mixed (Figures 3C, S8C): less than 3% changes in male and female WT aortas but 25% decreases and 17% increases in male and female MFS aortas, respectively, when BAPN was given from 4–8 weeks. By contrast, this stiffness increased ~10% in male and female WT and MFS mice when BAPN was given from 8–12 weeks. Results were similar in the axial direction, but less dramatic (Figures 3G, S8G). Hence, BAPN reduced circumferential stiffness in male MFS aortas only when BAPN was started at 4 weeks of age.

BAPN Differentially Affects Aortic Stress, Overall Survival, and Wall Strength

Aortic rupture occurs when wall stress exceeds strength. Many tacitly assume that wall stress is higher in dilated and aneurysmal arteries, but such stress results from a complex combination of inner radius, wall thickness, axial stretch, and physiological biaxial loading. Tail-cuff measured systolic blood pressures did not differ across groups. Again with $n = 5$ per group (Figure S1), values of wall stress were similar in male and female WT and MFS mice at both 8 (with circumferential values ~240–280 kPa) and 12 (~205–240 kPa) weeks of age (Figures 3D, S8D). There was, however, a 9–18% decrease in biaxial wall stress in male and female WT aortas when BAPN was given from 4–8 weeks and a 6–27% increase in WT aortas when BAPN was given from 8–12 weeks. By contrast (Figures 3D,H, S8D,H), there was a dramatic decrease in wall stress in MFS aortas when BAPN was given from 4–8 weeks (45–63% in males, 41–49% in females) and a similar though less dramatic decrease when given from 8–12 weeks (9–18%, slightly greater in males).

Gross examinations revealed spatial heterogeneity in the aortic phenotype, especially in the young male MFS aortas wherein particular regions dilated more (Figure 4A). Given that effects of BAPN were more dramatic when administered from 4–8 weeks of age, biomechanical metrics were re-evaluated independently in a sub-set of 8-week old male and female WT and MFS aortas, with and without BAPN ($n = 23$, Figure 4B). Panoramic digital image correlation (pDIC) and optical coherence tomography (OCT) measurements corroborated the standard biaxial data (cf. Figure 3) but revealed heterogeneous changes around the circumference and along the length of the ascending aorta (Figures 4B,C, S9–11). Again, values of circumferential material stiffness were higher in MFS compared to age- and sex-matched controls and affected little by BAPN. The OCT data revealed marked regional variations in wall thickness, particularly in the male MFS aorta. Given the need for pressurization, all of these data were collected for vessels that did not rupture *in vivo*.

Whereas all mice survived to the intended endpoint when BAPN was given from 8–12 weeks of age ($n = 49/49$; 13 MWT, 14 FWT, 12 MMFS, 10 FMFS), 55% (41/74) of WT mice and 92% (80/87) of MFS mice survived when given BAPN from 4–8 weeks (Figure 5A). Of the 41 surviving younger WT mice, 80% (33/41) were female and 20% (8/41) male. Recall that wall stress was lower than normal in the younger mice given BAPN, thus suggesting compromised wall strength. Burst-pressure tests on aortas from mice given BAPN from 4–8 weeks ($n = 21$; 6 MWT, 5 FWT, 5 MMFS, 5 FMFS) confirmed significantly lower values for male WT aortas and a trend toward lower values for female WT aortas. Conversely, burst pressures were higher, not lower, in aortas from age-matched male and female MFS mice (Figure 5C). Examination of these vessels (recall Figure 5B) revealed further that *ex vivo* rupture tended to occur more distally and along the inner curvature in WT aortas, but more proximally and ventrally in MFS aortas (Figure 5D,E). Moreover, rupture sites in MFS aortas with BAPN given from 4–8 weeks (Figures 5F, S13) tended to locate in regions with substantial dilatation (mostly >50% increase in local radius) but less thickening (mostly <50% increase in local thickness), suggesting locally elevated wall stresses relative to bulk values.

BAPN Differentially Affects Collagen Fibril Properties

Because collagen fibers endow the aortic wall with most of its strength, and the younger mice had greater vulnerability to lethal rupture, we evaluated collagen integrity in the 4–8 week old groups using picro-sirius stained histological sections, second harmonic generation in multiphoton microscopy, and transmission electron microscopy. Viewing picro-sirius red stained sections ($n = 5 - 8$ per each of the 8 groups; Table S1) under polarized light (Figure 6A–D) revealed little change in collagen in male WT mice without or with 4-weeks of BAPN, but higher staining in male MFS mice particularly following the 4-weeks of BAPN. Interestingly, there was also an increase in the ratio of thick:thin collagen fibers in the adventitia, with a greater increase in thick fibers in male MFS mice. Immuno-staining for LOX revealed that this important cross-linking enzyme was initially highest in the male MFS aortas and lowest in male WT prior to BAPN; this difference persisted following BAPN, though at lower levels (Figure 6A,B,E).

Second harmonic generation in non-fixed physiologically loaded sections suggested further that the straightness of adventitial collagen fibers tended not to change with BAPN given from 4–8 weeks ($n = 17$; 4 MWT and 1 FWT without BAPN, 0 MWT and 4 FWT with BAPN, 3 MMFS and 1 FMFS without BAPN, 2 MMFS and 2 FMFS with BAPN), but micron-scale collagen fiber bundle widths reduced (Figure 7A) consistent with picro-sirius red findings. Transmission electron micrographs of fixed sections ($n = 50$; 17 MWT, 15 FWT, 10 MMFS, 8 FMFS) for the same groups (Figure 7B) revealed, among other nanoscale findings, that there was no statistically significant pairwise differences in collagen fibril cross-sectional shape based on aspect ratio, which was 1.3±0.2 across all 8 of the 4–8 week groups (Figure 7C). Mean fibril cross-sectional area was higher, however, and more variable in MFS aortas compared to WT counterparts; mean fibril area also tended to be larger in female than in male WT mice regardless of BAPN, though this difference may have reached statistical significance with BAPN due to higher sample sizes (Figure 7D). Importantly, the overall area fraction occupied by collagen fibrils in the adventitia decreased dramatically in male WT mice (Figure 7E). Detailed assessments of distributions of fibril cross-sections for all 8 of the 4–8 week groups confirmed these mean findings while suggesting a pre-existing vulnerability in the male WT aortas (Figure 7F,G). Regardless, macro-scale burst pressures (strength), the lowest of which was in the young male WT aortas (recall Figure 5C), correlated well with adventitial collagen fibril cross-sectional area (Figure 7H).

DISCUSSION

It has been known since the 1950s that BAPN can compromise the structural integrity of the aorta, with younger rodents more vulnerable than older rodents. Most recent studies have given BAPN either to young (often 3 wks old) or hypertensive older (often 8 wks old or older) mice[17]. BAPN blocks crosslinking of newly synthesized elastic and collagen fibers, hence these protocols have proven useful because extracellular matrix synthesis is high in the developing aorta[30] and hypertension increases collagen synthesis in the mature aorta[31]. Collagen turnover is also likely increased in cases of rapid aneurysmal enlargement[32,33]. A prior study comparing WT and *Fbn1*$^{C1041G/+}$ MFS mice (presumably males, but sex was not indicated) showed that the ascending aorta, but not aortic root, dilated after 4 and especially 8 weeks of BAPN when started in 6-week old MFS, but not in age-matched WT, mice[16]. Our findings for male mice given BAPN from 4–8 weeks of age are generally consistent with these prior findings despite the difference in the age at which BAPN was started. Importantly, we further found BAPN-induced dilatation to be absent in young female WT mice and modest in young female MFS mice, and that all findings were attenuated in older mice (when BAPN was given from 8–12 weeks of age, after the aorta is biomechanically mature and collagen turnover rates are likely lower[18,34,35]). That is, young male MFS mice were most susceptible to BAPN-exaggerated dilatation of the ascending aorta with associated reductions in biomechanical function (mainly lower *in vivo* axial stretch and elastic energy storage, which arise mainly from elastic fibers).

Yet, elastic fiber area inferred via Movat staining, which is dominated by the elastic lamellae, remained similar when we initiated BAPN at 4 weeks of age, just after biomechanical maturation of the load-carrying lamellae in WT mice[18,34,35]. Given a prior report of unremarkable gross changes in elastic lamellae in the young rat aorta following BAPN[35], and a recently identified strong correlation between aortic dilatation and elastin porosity in MFS[5], we used two-photon fluorescence to examine elastin porosity in a small sub-set of mixed sex mice (Figure S1). Marked increases in elastin porosity and pore size emerged in MFS aortas when BAPN was given from 4–8 weeks, especially in males (Figure S15), which had the greatest aortic dilatation. These changes in porosity were greatest in the inner and outer media, with the former perhaps contributing more to dilatation[25]. Hence, consistent with a prior non-BAPN study in *Fbn1*$^{C1041G/+}$ and *Fbn1*$^{mgR/mgR}$ mice[5], increased BAPN-associated dilatation correlated well with increased elastin porosity (Graphical Abstract).

There was no report of increased mortality in *Fbn1*$^{C1041G/+}$ mice given BAPN in the prior study[16], and low mortality in ours. Rather, overall BAPN-associated mortality was much greater in young littermate WT (*Fbn1*$^{+/+}$) than young MFS (*Fbn1*$^{C1041G/+}$) mice, namely 45% versus 8%, seemingly consistent with an early compensatory accumulation and/or cross-linking of collagen in this MFS model[16]. We previously found increased adventitial collagen in another mouse model of thoracic aortopathy (conditional *Tgfbr1r2* knockout in adults) that appeared to protect against *in vivo* rupture[27]. Most of the WT mice that died (presumably of aortic rupture) herein were young males: 77% (27/35) of the males but only 15% (6/39) of the females died when given BAPN from 4–8 weeks of age. Particularly important, *ex vivo* burst-pressures were slightly (but not significantly) higher in WT aortas compared with MFS aortas, but this trend reversed following BAPN; burst-pressure became lowest in aortas from BAPN-exposed WT males. Regions of failure during *ex vivo* testing included the inner and outer curvature and more ventral aspect of the ascending aorta – distally for WT and proximally for MFS aortas. Regions of *ex vivo* failure in the MFS aorta tended to coincide with those that experienced local dilatation (increased radius) without substantial thickening, suggesting that compensatory remodeling is needed to protect the aorta from rupture.

BAPN was previously used to offset measured increases in *Lox* and *Loxl1* in *Fbn1*$^{C1041G/+}$ aortas relative to WT controls, with results suggesting that increased LOX is compensatory in this MFS model[16], perhaps contributing to its slow aneurysmal enlargement. Our results from immuno-staining were similar: LOX was lowest in aortas from WT males, both without and with BAPN, and highest in aortas from MFS males. Additionally, LOX trended higher in young female WT compared to age-matched male WT mice and was generally higher in MFS than WT mice independent of age or sex. Given that LOX is a strong cross-linker of collagen, which endows the wall with stiffness and strength, we used three methods to further examine collagen integrity. The larger ratio of thick:thin adventitial collagen fibers (PSR) following 4–8 weeks of BAPN, especially in MFS and independent of sex, suggested that previously cross-linked thick fibers are more stable than thin fibers. Micron-scale reductions in adventitial collagen bundle width (second harmonic generation) were similar in both the rupture-prone young male WT mice and the less-prone young male MFS mice whereas nanometer-scale adventitial collagen fibril density (transmission electron microscopy) was lower in young male WT than young male MFS aortas. Whereas thoracic aortic aneurysms exhibit an increased circumferential material stiffness[25,26], it is not clear whether this increase is pathologic or protective. Effects of BAPN on circumferential stiffness were modest when BAPN was started at 4 weeks of age with little effect when initiated at 8 weeks of age in the MFS mice. These results suggest that effects of BAPN on collagen are primarily in reducing strength, not stiffness, perhaps with the former depending more on inter- and intra-molecular cross-links at the fibril level and the latter more on macroscale fiber undulation.

The strong sexual dimorphism manifested both as greater BAPN-induced dilatation in young male vs. female MFS mice and as greater BAPN-induced lethality in young male vs. female WT mice. Notably, our choice to start BAPN at 4 weeks of age is just after estrus begins in female mice (~P26). Although estrogen increases LOX in diverse connective tissues[36,37], a recent study using angiotensin II suggested that greater aortopathy in males is due to the androgens[38]. Notably, orchiectomy vs. ovariectomy studies suggest that androgens reduce LOX in male WT aortas, hence rendering them vulnerable mechanically[39]. Conversely, an elastase+BAPN model of abdominal aortic aneurysms reported greater dilatation in female than male mice, though with low numbers of females[40]. There is a need for further study of sex differences in aortopathy, particularly given the sexual dimorphism in aortic dissection in humans, wherein males are limiat greater risk than females[41] similar to our findings herein.

Limitations:

Notwithstanding lessons learned herein, much remains to be understood. BAPN causes dilatation of the ascending aorta, but not aortic root, in $Fbn1^{C1041G/+}$ mice[16]. We focused on the affected segment, but there is need to delineate effects of BAPN on these two regions of the proximal aorta, which derive from different embryonic origins. Unfortunately, our method of cannulation precludes a rigorous biaxial study of the aortic root in mice. This prior study also showed that losartan attenuated the BAPN-exaggerated aortopathy[16]. Other drugs (including mTOR inhibitors) have also attenuated effects of BAPN on the aorta[42], thus a comparative study could provide further insight into mechanisms of progressive aortopathy and its treatment. There is also a need to understand better the possible roles of intramural glycosaminoglycans, which increase following BAPN[35,43] and have been implicated in dissection and rupture of the thoracic aorta[44]. Consistent with prior studies, we found diffuse accumulations of mucoid material in MFS aortas, which was increased by BAPN. That this increase did not increase rupture potential in MFS reminds us of the key difference between diffuse (as seen herein) and pooled glycosaminoglycans, with the latter creating stress concentrations that appear to nucleate intramural delaminations that lead to dissection. Finally, histological and biomechanical studies are necessarily descriptive;

no current micromechanical theories explain precisely how microstructural architecture translates to tissue-level mechanical properties. We thus employed multiple approaches for histological examination (over micron to nanometer scales) and biomechanical phenotyping (bulk and regional) to cross-validate findings and increase insight. We did not attempt to identify underlying molecular mechanisms by which the age and sex differences emerged; such mechanisms will need to be identified to identify targets for therapies.

In summary, notwithstanding the critical role of compromised elastic fiber integrity in initiating lesion progression in MFS[5], the mechanical functionality of collagen fibers and rates of turnover are critical modulators of acute outcomes – dissection and rupture. Although BAPN exacerbated dilatation of MFS aortas when started at 4 weeks of age, it appears that prior compensatory increases in collagen and its LOX-mediated cross-linking prevented most of these aortas from progressing to rupture during the 4-week study. By contrast, BAPN did not induce aneurysmal dilatation in WT aortas; rather, it increased rupture-potential, especially in male mice, the aortas of which exhibited the lowest LOX staining and lowest adventitial collagen fibril density. Although thoracic aortic aneurysms, dissections, and rupture are typically discussed together, the present data suggest different biomechanical mechanisms of dilatation (related to compromised elastic fibers), mostly in male MFS mice, and transmural rupture (related to compromised collagen fibrils, especially adventitial), mostly in male WT mice. There is, therefore, motivation to develop improved micromechanical computational models to better understand these failures while molecular mechanisms are needed to guide the development of pharmacotherapies that attenuate losses in competent elastic fibers and preserve or promote collagen fibril integrity.

Supplementary Material

Refer to Web version on PubMed Central for supplementary material.

Sources of Funding

This work was supported by grants from the NIH (P01 HL134605, U01 HL142518, R01 HL168473) and Leducq Foundation (erAADicate).

Nonstandard Abbreviations and Acronyms

BAPN	β-aminopropionitrile
FMFS	female Marfan syndrome mice
FWT	female wild-type mice
HBSS	Hank’s buffered saline solution
LOX	lysyl oxidase
MFS	Marfan syndome
MMFS	male Marfan syndrome mice
MWT	male wild-type mice

OCT	optical coherence tomography
pDIC	panoramic digital image correlation
SD	standard deviation
WT	wild-type

REFERENCES

1. Pearson GD, Devereux R, Loeys B, Maslen C, Milewicz D, Pyeritz R, Ramirez F, Rifkin D, Sakai L, Svensson L. Report of the national heart, lung, and blood institute and national marfan foundation working group on research in marfan syndrome and related disorders. Circulation. 2008;118:785–791. [PubMed: 18695204]
2. Ramirez F, Dietz HC. Fibrillin-rich microfibrils: Structural determinants of morphogenetic and homeostatic events. Journal of cellular physiology. 2007;213:326–330. [PubMed: 17708531]
3. Pereira L, Lee SY, Gayraud B, Andrikopoulos K, Shapiro SD, Bunton T, Biery NJ, Dietz HC, Sakai LY, Ramirez F. Pathogenetic sequence for aneurysm revealed in mice underexpressing fibrillin-1. Proceedings of the National Academy of Sciences. 1999;96:3819–3823.
4. Judge DP, Biery NJ, Keene DR, Geubtner J, Myers L, Huso DL, Sakai LY, Dietz HC. Evidence for a critical contribution of haploinsufficiency in the complex pathogenesis of Marfan syndrome. The Journal of clinical investigation. 2004;114:172–181. [PubMed: 15254584]
5. Cavinato C, Chen M, Weiss D, Ruiz-Rodríguez MJ, Schwartz MA, Humphrey JD. Progressive Microstructural Deterioration Dictates Evolving Biomechanical Dysfunction in the Marfan Aorta. Frontiers in cardiovascular medicine. 2021:1904.
6. Gharraee N, Sun Y, Swisher JA, Lessner SM. Age and sex dependency of thoracic aortopathy in a mouse model of marfan syndrome. American Journal of Physiology-Heart and Circulatory Physiology. 2022;322:H44–H56. [PubMed: 34714692]
7. Humphrey JD, Tellides G. Central artery stiffness and thoracic aortopathy. American Journal of Physiology-Heart and Circulatory Physiology. 2019;316:H169–H182. [PubMed: 30412443]

. Humphrey JD, Schwartz MA, Tellides G, Milewicz DM. Role of mechanotransduction in vascular biology: focus on thoracic aortic aneurysms and dissections. Circulation research. 2015;116:1448–1461. [PubMed: 25858068]

9. Latorre M, Humphrey J. Numerical knockouts–In silico assessment of factors predisposing to thoracic aortic aneurysms. PLoS computational biology. 2020;16:e1008273. [PubMed: 33079926]
10. Powell JT, Länne T. Through thick and thin collagen fibrils, stress, and aortic rupture: another piece in the jigsaw. In: Am Heart Assoc; 2007:2687–2688.
11. Zilberberg L, Phoon CK, Robertson I, Dabovic B, Ramirez F, Rifkin DB. Genetic analysis of the contribution of LTBP-3 to thoracic aneurysm in Marfan syndrome. Proceedings of the National Academy of Sciences. 2015;112:14012–14017.
12. Pedroza AJ, Tashima Y, Shad R, Cheng P, Wirka R, Churovich S, Nakamura K, Yokoyama N, Cui JZ, Iosef C. Single-cell transcriptomic profiling of vascular smooth muscle cell phenotype modulation in Marfan syndrome aortic aneurysm. Arteriosclerosis, thrombosis, and vascular biology. 2020;40:2195–2211. [PubMed: 32698686]
13. Ferruzzi J, Collins MJ, Yeh AT, Humphrey JD. Mechanical assessment of elastin integrity in fibrillin-1-deficient carotid arteries: implications for Marfan syndrome. Cardiovascular research. 2011;92:287–295. [PubMed: 21730037]
14. Brüel A, Ørtoft G, Oxlund H. Inhibition of cross-links in collagen is associated with reduced stiffness of the aorta in young rats. Atherosclerosis. 1998;140:135–145. [PubMed: 9733224]
15. Rodríguez C, Martínez-González J, Raposo B, Alcudia JF, Guadall A, Badimon L. Regulation of lysyl oxidase in vascular cells: lysyl oxidase as a new player in cardiovascular diseases. Cardiovascular research. 2008;79:7–13. [PubMed: 18469024]
16. Busnadiego O, Del Blanco DG, González-Santamaría J, Habashi J, Calderon J, Sandoval P, Bedja D, Guinea-Viniegra J, Lopez-Cabrera M, Rosell-Garcia T. Elevated expression levels of lysyl

oxidases protect against aortic aneurysm progression in Marfan syndrome. Journal of molecular and cellular cardiology. 2015;85:48–57. [PubMed: 25988230]

17. Zheng H-q Rong J-b, Ye F-m Xu Y-c, Lu HS Wang J-a. Induction of thoracic aortic dissection: a mini-review of β-aminopropionitrile-related mouse models. Journal of Zhejiang University-SCIENCE B. 2020;21:603–610. [PubMed: 32748576]
18. Murtada SI, Kawamura Y, Li G, Schwartz MA, Tellides G, Humphrey JD. Developmental origins of mechanical homeostasis in the aorta. Developmental Dynamics. 2021;250:629–639. [PubMed: 33341996]
19. Ferruzzi J, Bersi M, Humphrey J. Biomechanical phenotyping of central arteries in health and disease: advantages of and methods for murine models. Annals of biomedical engineering. 2013;41:1311–1330. [PubMed: 23549898]
20. Bersi MR, Bellini C, Di Achille P, Humphrey JD, Genovese K, Avril S. Novel methodology for characterizing regional variations in the material properties of murine aortas. Journal of biomechanical engineering. 2016;138:071005.
21. Weiss D, Cavinato C, Gray A, Ramachandra AB, Avril S, Humphrey JD, Latorre M. Mechanics-driven mechanobiological mechanisms of arterial tortuosity. Science Advances. 2020;6:eabd3574. [PubMed: 33277255]
22. Rego BV, Weiss D, Bersi MR, Humphrey JD. Uncertainty quantification in subject-specific estimation of local vessel mechanical properties. International Journal for Numerical Methods in Biomedical Engineering. 2021;37:e3535. [PubMed: 34605615]
23. Genovese K, Lee Y, Lee A, Humphrey J. An improved panoramic digital image correlation method for vascular strain analysis and material characterization. Journal of the mechanical behavior of biomedical materials. 2013;27:132–142. [PubMed: 23290821]
24. Schroeder F, Polzer S, Slažanský M, Man V, Skácel P. Predictive capabilities of various constitutive models for arterial tissue. Journal of the mechanical behavior of biomedical materials. 2018;78:369–380. [PubMed: 29220821]
25. Bellini C, Bersi M, Caulk A, Ferruzzi J, Milewicz D, Ramirez F, Rifkin D, Tellides G, Yanagisawa H, Humphrey J. Comparison of 10 murine models reveals a distinct biomechanical phenotype in thoracic aortic aneurysms. Journal of The Royal Society Interface. 2017;14:20161036. [PubMed: 28490606]
26. Bersi MR, Bellini C, Humphrey JD, Avril S. Local variations in material and structural properties characterize murine thoracic aortic aneurysm mechanics. Biomechanics and modeling in mechanobiology. 2019;18:203–218. [PubMed: 30251206]
27. Kawamura Y, Murtada S-I, Gao F, Liu X, Tellides G, Humphrey J. Adventitial remodeling protects against aortic rupture following late smooth muscle-specific disruption of TGFβ signaling. Journal of the Mechanical Behavior of Biomedical Materials. 2021;116:104264. [PubMed: 33508556]
28. Rego BV, Weiss D, Humphrey JD. A fast, robust method for quantitative assessment of collagen fibril architecture from transmission electron micrographs. bioRxiv. 2023:2023.2002. 2006.527383.
29. Otsu N A threshold selection method from gray-level histograms. IEEE transactions on systems, man, and cybernetics. 1979;9:62–66.
30. Kelleher CM, McLean SE, Mecham RP. Vascular extracellular matrix and aortic development. Current topics in developmental biology. 2004;62:153–188. [PubMed: 15522742]
31. Nissen R, Cardinale GJ, Udenfriend S. Increased turnover of arterial collagen in hypertensive rats. Proceedings of the National Academy of Sciences. 1978;75:451–453.
32. Weiss D, Latorre M, Rego B, Cavinato C, Tanski B, Berman A, Goergen C, Humphrey J. Biomechanical consequences of compromised elastic fiber integrity and matrix cross-linking on abdominal aortic aneurysmal enlargement. Acta biomaterialia. 2021;134:422–434. [PubMed: 34332103]
33. Wilson J, Baek S, Humphrey J. Parametric study of effects of collagen turnover on the natural history of abdominal aortic aneurysms. Proceedings of the Royal Society A: Mathematical, Physical and Engineering Sciences. 2013;469:20120556.

34. Gerrity R, Cliff W. The aortic tunica media of the developing rat. I. Quantitative stereologic and biochemical analysis. Laboratory investigation; a journal of technical methods and pathology. 1975;32:585–600. [PubMed: 1127878]
35. Nakashima Y, Sueishi K. Alteration of elastic architecture in the lathyritic rat aorta implies the pathogenesis of aortic dissecting aneurysm. The American journal of pathology. 1992;140:959. [PubMed: 1562054]
36. Sanada H, Shikata J, Hamamoto H, Ueba Y, Yamamuro T, Takeda T. Changes in collagen cross-linking and lysyl oxidase by estrogen. Biochimica et Biophysica Acta (BBA)-General Subjects. 1978;541:408–413. [PubMed: 27234]
37. Wei S, Gao L, Wu C, Qin F, Yuan J. Role of the lysyl oxidase family in organ development. Experimental and Therapeutic Medicine. 2020;20:163–172.
38. Zhang X, Thatcher S, Wu C, Daugherty A, Cassis LA. Castration of male mice prevents the progression of established angiotensin II-induced abdominal aortic aneurysms. Journal of vascular surgery. 2015;61:767–776. [PubMed: 24439319]
39. Okuyama M, Jiang W, Javidan A, Chen JZ, Howatt DA, Yang L, Hamaguchi M, Yasugi T, Aono J, Vazquez-Padron RI. Lysyl oxidase inhibition ablates sexual dimorphism of abdominal aortic aneurysm formation in mice. Circulation. 2020;142:1993–1995. [PubMed: 33196308]
40. Berman AG, Romary DJ, Kerr KE, Gorazd NE, Wigand MM, Patnaik SS, Finol EA, Cox AD, Goergen CJ. Experimental aortic aneurysm severity and growth depend on topical elastase concentration and lysyl oxidase inhibition. Scientific reports. 2022;12:1–13. [PubMed: 34992227]
41. LeMaire SA, Russell L. Epidemiology of thoracic aortic dissection. Nature reviews cardiology. 2011;8:103–113. [PubMed: 21173794]
42. Zhou B, Li W, Zhao G, Yu B, Ma B, Liu Z, Xie N, Fu Y, Gong Z, Dai R. Rapamycin prevents thoracic aortic aneurysm and dissection in mice. Journal of Vascular Surgery. 2019;69:921–932. e923. [PubMed: 30253896]
43. Hosoda Y, Iri H. 1. A histological and histochemical study on successive changes of the lathyritic rat aorta. Pathology International. 1966;16:239–252.
44. Cikach FS, Koch CD, Mead TJ, Galatioto J, Willard BB, Emerton KB, Eagleton MJ, Blackstone EH, Ramirez F, Roselli EE. Massive aggrecan and versican accumulation in thoracic aortic aneurysm and dissection. JCI insight. 2018;3.

Highlights

Biomechanical mechanisms of aortic dilatation relate mainly to compromised elastic fibers while those of rupture relate mainly to compromised collagen fibrils, especially adventitial.

A strong sexual dimorphism manifests both as greater BAPN-induced aortic dilatation in young male vs. female Marfan mice and greater BAPN-induced lethality in young male vs. female wild-type mice.

Compensatory increases in mural collagen and its LOX-mediated cross-linking protect the otherwise vulnerable *Fbn1*$^{C1041G/+}$ Marfan aorta from early rupture.

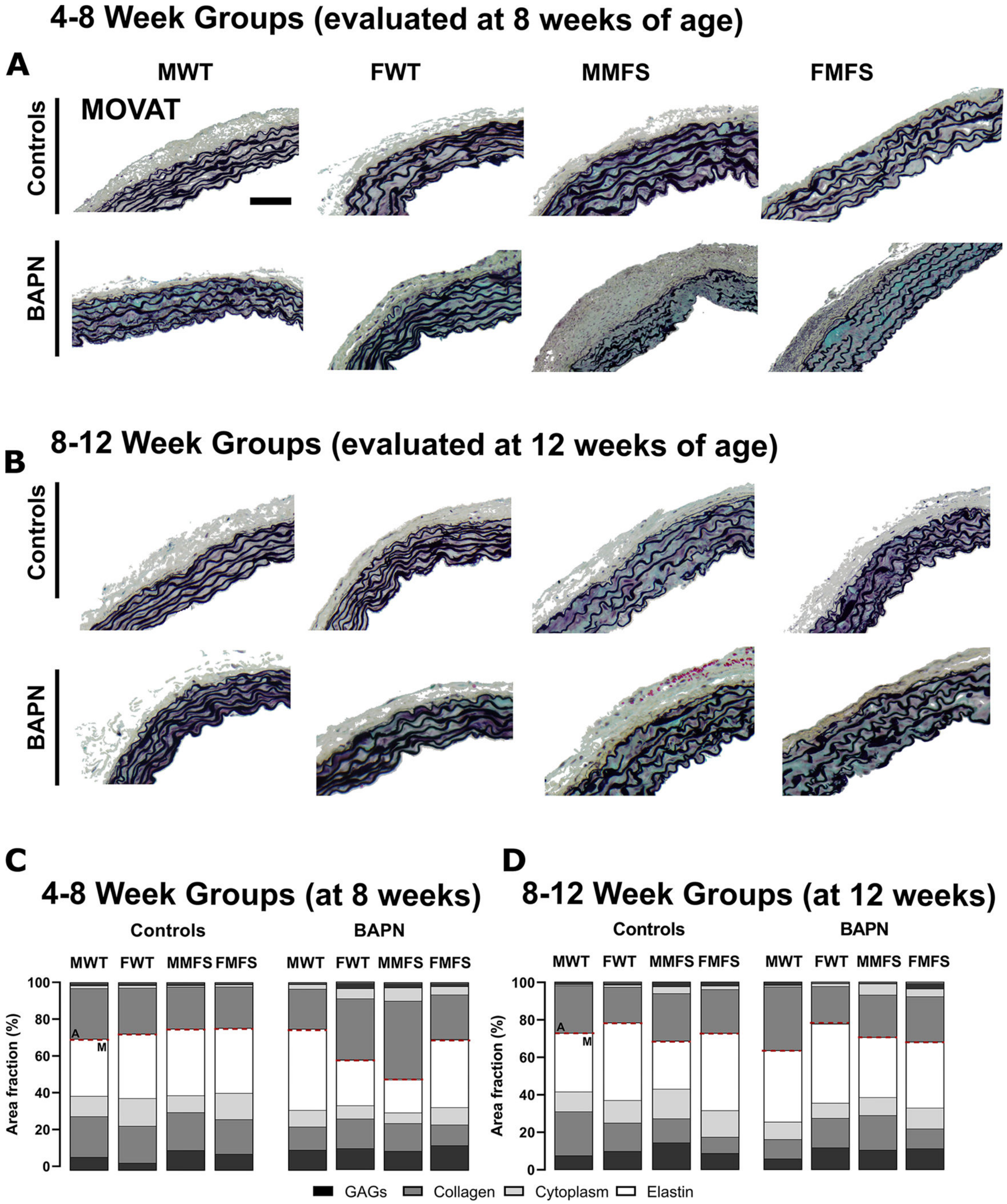

Figure 1.

A, B. Representative portions of Movat-stained histological cross-sections from all 16 groups: 4–8 week old (evaluated at 8 weeks) and 8–12 week old (evaluated at 12 weeks), male (M) and female (F), wild-type (WT) and Marfan syndrome (MFS), without (controls) and with BAPN given for 4 weeks. Elastic fibers in black, glycosaminoglycans in blue/aqua, collagen in yellow/brown. Scale bar = 100 μm. C, D. Representative mural percentages (*n* = 3 randomly selected per group for standard histology, with 3 technical replicates each) separated by medial (M) and adventitial (A) layers (dashed horizontal line of separation).

Qualitatively, note the marked increase in adventitial fraction in the young male MFS aortas following BAPN. See also Figure S6.

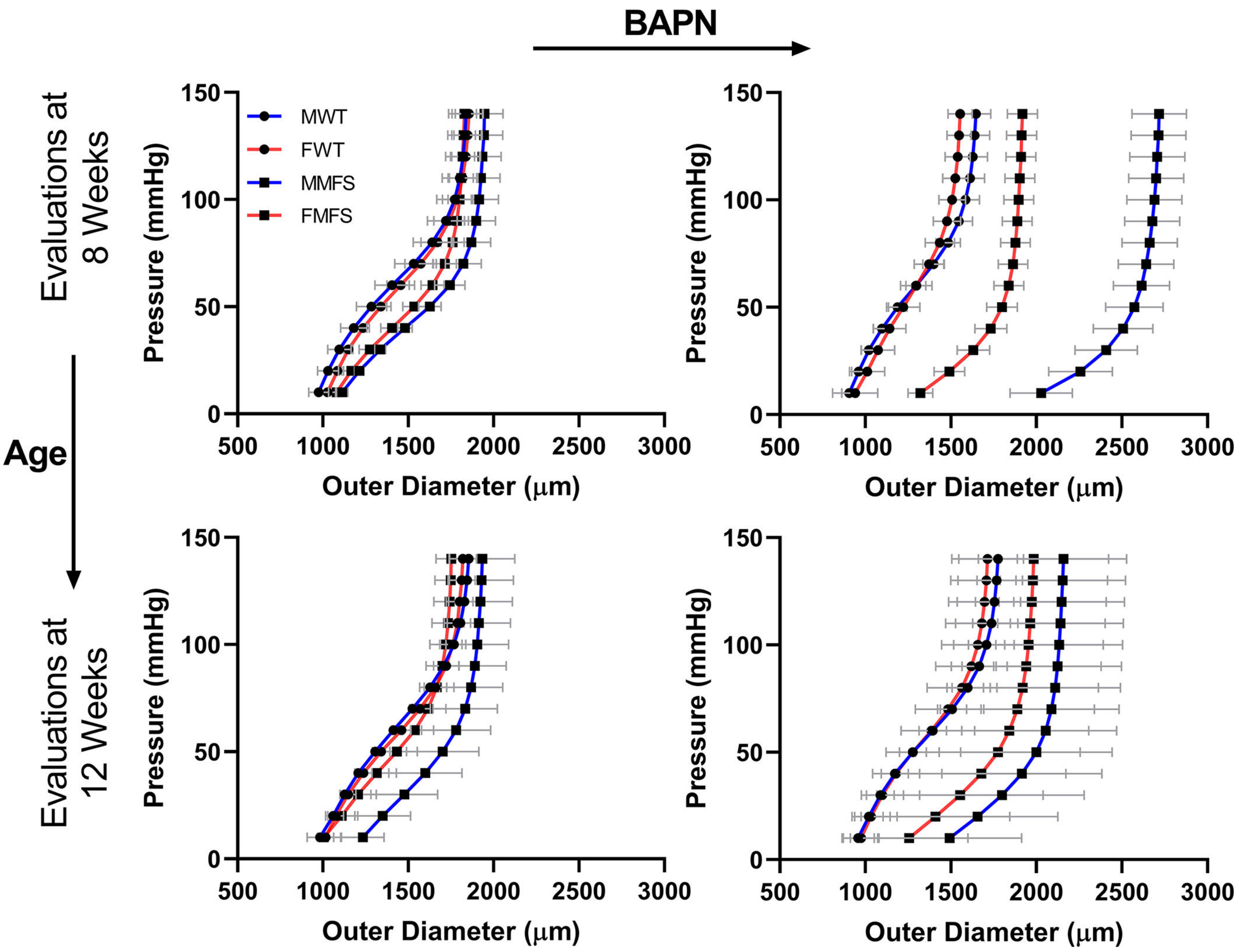

Figure 2.

Pressure-diameter behaviors (mean±SD) of the ascending aorta for all 16 Groups ($n = 5$ each, thus representing 80 specimens): female (F) and male (M), wild-type (WT) and Marfan syndrome (MFS) mice without (left) and with (right) BAPN given for 4 weeks beginning either at 4 weeks of age (then evaluated at 8 weeks) or 8 weeks of age (evaluated at 12 weeks of age), with age- and sex-matched controls not receiving BAPN. Qualitatively, BAPN increased aortic dilatation more in MFS than in WT, more in M than F, and more when BAPN was initiated at 4 than 8 weeks of age. These results are not compared statistically since they show a visually interpretable subset of the full data set (namely, circumferential structural data from 1 of the 7 biaxial testing protocols, with only 14 of the over 100 states per protocol per vessel shown for clarity). See Figure S7 for associated circumferential stress-stretch behaviors, and Figures 3, S8 for quantitation and statistical comparisons of the full data sets.

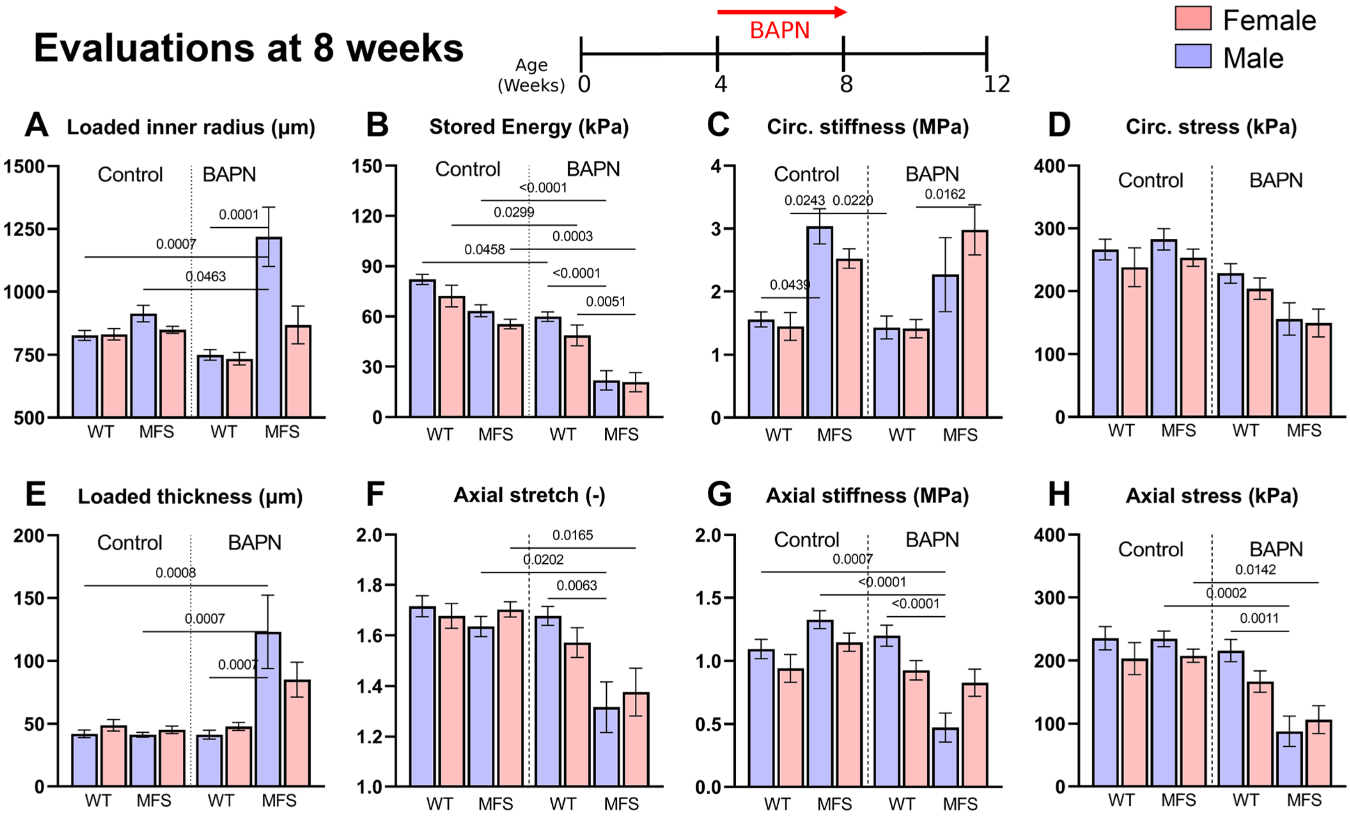

Figure 3.

A-H. Comparison of 8 key geometric and mechanical metrics for the 8 younger Groups: female (F) and male (M), wild-type (WT) and Marfan syndrome (MFS) ascending aortas without (control) or with BAPN given for 4 weeks beginning at 4 weeks of age (then evaluated at 8 weeks). See Figure S8 for similar results when BAPN was started at 8 weeks of age (evaluated at 12 weeks of age). These values (mean±SD) were inferred from *ex vivo* mechanical testing of excised segments (with $n = 5$ per group, 40 aortas tested over the 8 overall groups of younger mice) under physiological conditions, with each mechanical metric calculated from biaxial data from 7 cyclic loading protocols that yielded over 2800 data points per each of the 40 vessels (i.e., comparisons of each metric are based on 112000 on-line computer-controlled measurements). Statistical comparisons by non-parametric Kruskal Wallis test followed by Dunn's post-hoc test for multiple comparisons; p values < 0.05 indicated.

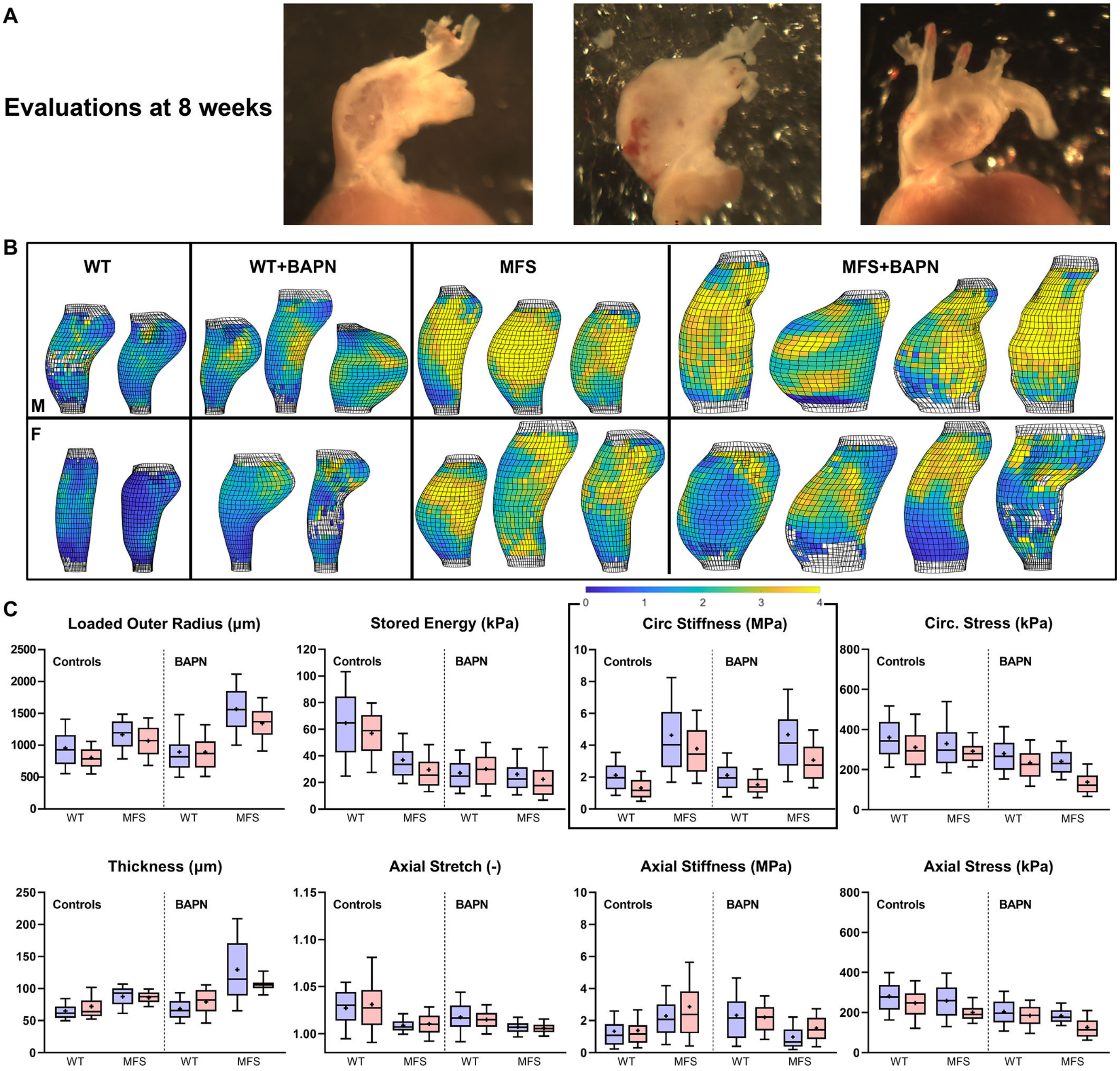

Figure 4.

A. Illustrative gross images of three male MFS aortas following 4 weeks of BAPN that started at 4 weeks of age (then evaluated at 8 weeks of age). Note the marked regional thinning of the wall even though these vessels did not rupture *in vivo*. B, C. Multimodal (pDIC + OCT) *ex vivo* testing under physiological loading confirmed findings from standard biaxial testing in a randomly selected sub-set of 8-week old male (M) and female (F) mice (*n* = 23 of 40), but further revealed regional heterogeneities in most geometric and mechanical metrics (see Figs S9–S12 for sample-specific distributions). Highlighted in panel B, for illustrative purposes, is the perhaps surprising lack of a dramatic effect of *in vivo* BAPN on circumferential material stiffness – with a colorimetric scale bar given from ~0 (darkest blue) to > 4 (yellow) MPa. Each bar and whisker plot represents ~2000 to 4000 data points, that is, ~1000 results around the circumference and along the length of each specimen, thus ~23000 data points are represented and compared within each of these 8 panels.

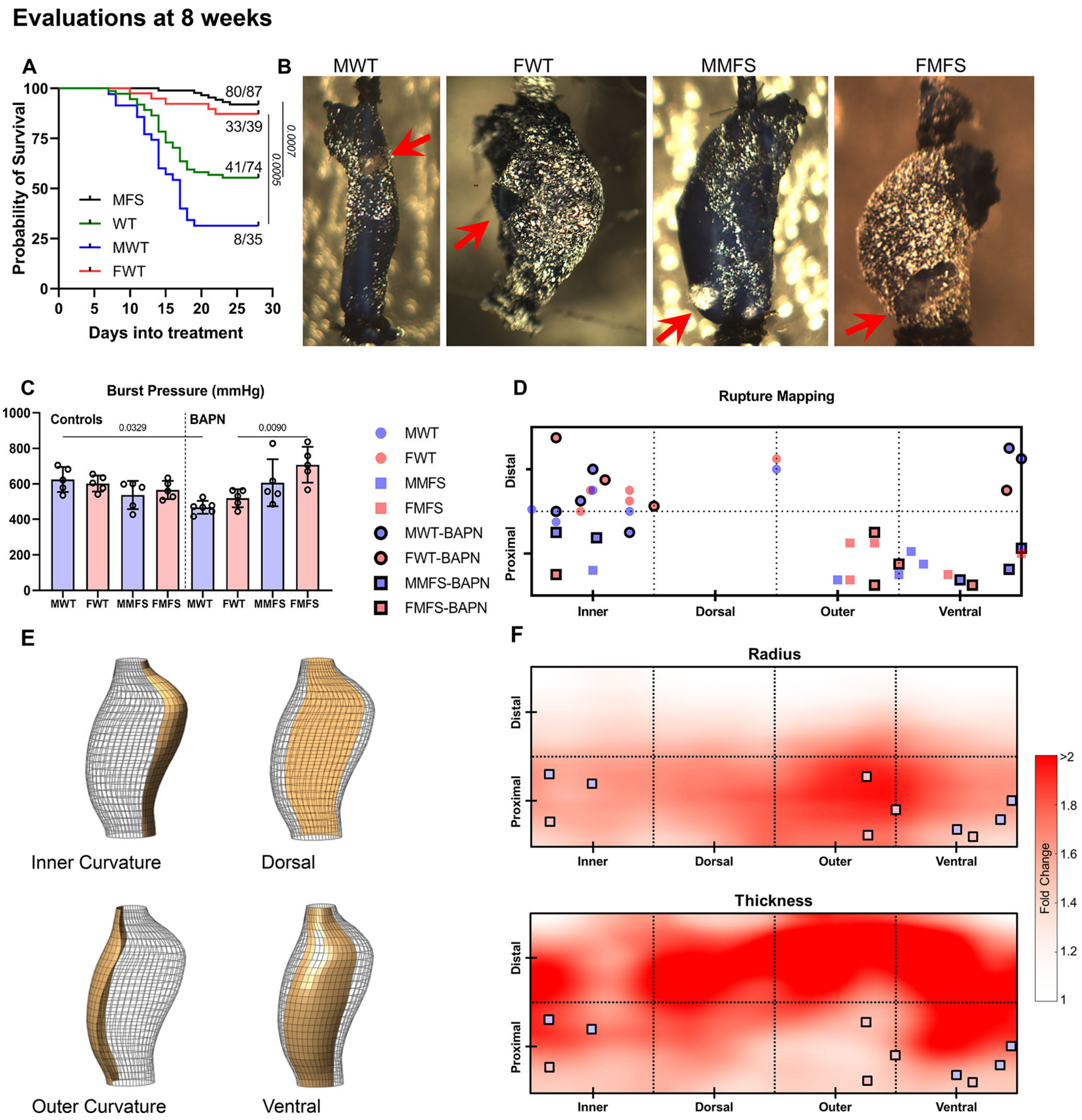

Figure 5.

A. Survival curves reveal a statistically higher BAPN-associated lethality in young WT than in young MFS mice, particularly in males (27/35 male WT mice died, 2/42 male MFS mice died). All recorded deaths were natural and mice were not necropsied to determine cause of death. B, C. Albeit restricted to aortas from surviving mice, *ex vivo* burst-pressure testing (mean±SD) confirmed greatest vulnerability in the young male WT aortas (red arrows indicate rupture sites). D, E. Rupture sites mapped onto four circumferential (inner curvature, dorsal, outer curvature, and ventral) and two axial (proximal half vs. distal half) regions. F. Maps show spatial fold-changes of radius and thickness associated with MFS and BAPN relative to the non-exposed WT controls (see Figure S13 for separate effects of sex, genotype, and BAPN). Dilatation in the MFS-BAPN group was observed primarily in proximal regions, particularly near the outer curvature, while thickening was mostly observed distally. Locations of failure during *ex vivo* testing of MFS aortas tended to coincide with regions that experienced local dilatation (i.e., increased radius) without substantial thickening.

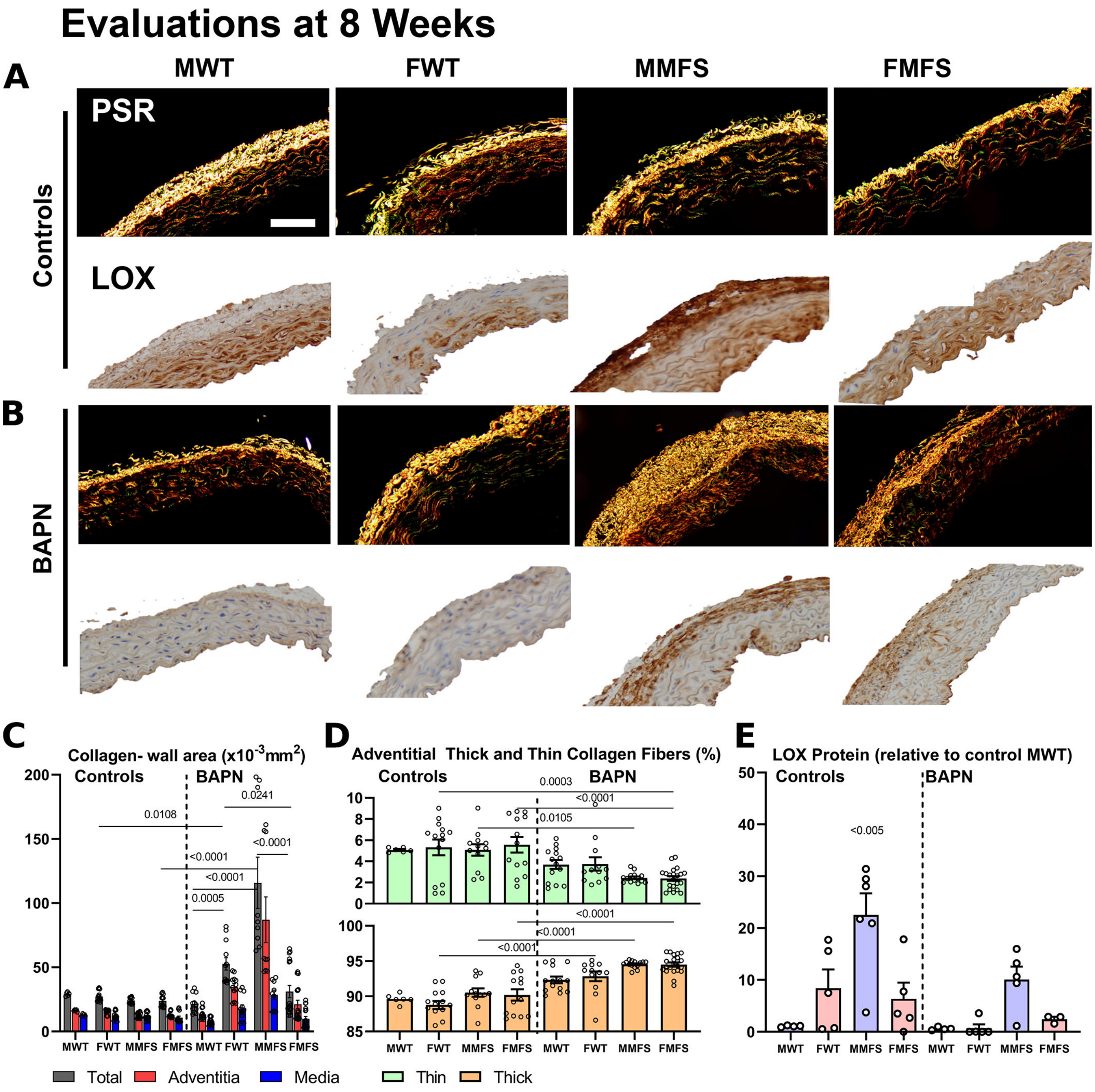

Figure 6.

A-D. Picro-sirius red stained cross-sections suggested modest changes in mural collagen following BAPN in older mice (not shown) as well as in most younger mice with the stark exception of young male MFS mice in which there was a marked increase in adventitial collagen. BAPN increased the ratio of thick:thin adventitial collagen in all young mice, perhaps due to a reduced incorporation of thin fibers during turnover. Scale bar = 100 μm. E. Notably, immuno-staining for LOX revealed generally higher levels in female than male mice, and higher levels in MFS than WT mice prior to BAPN. These levels tended to drop following BAPN although group-to-group trends persisted. Data are presented as means±SEM; statistical comparisons by non-parametric Kruskal Wallis test followed by Dunn's post-hoc test for multiple comparisons; noting that all statistical comparisons with the controls MMFS group were found significant (noting on the graph as <0.005).

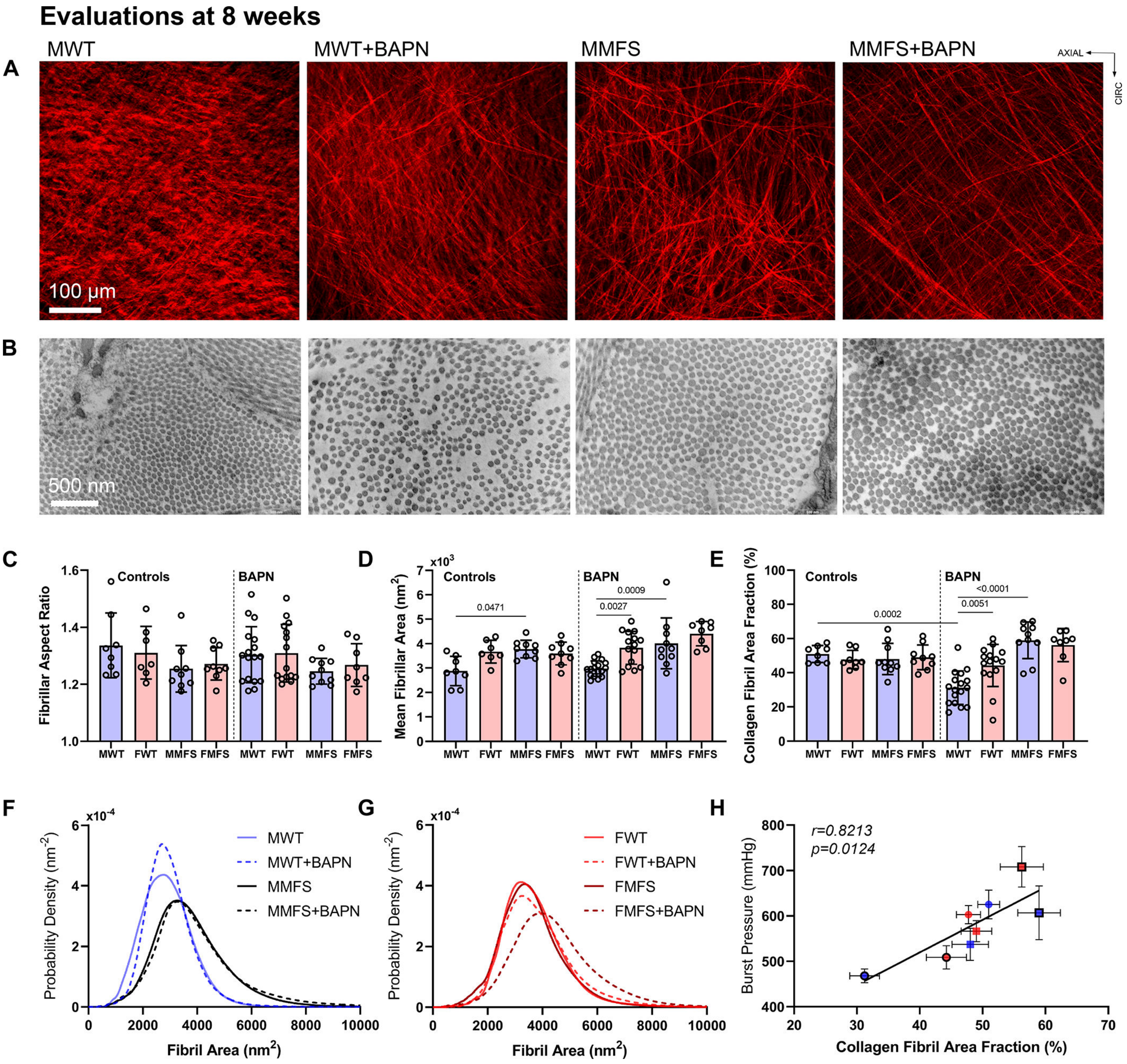

Figure 7.

A. Second harmonic generation for collagen fibers (red) during multiphoton microscopic examination (micron scale) of a sub-set of aortas from 8-week old mice confirmed reduced bundle diameters following BAPN (significant for WT) without changes in fiber straightness. B-E. Transmission electron microscopy (nanometer scale) further revealed, in a sub-set of aortas from 8-week old mice, similar collagen fibril cross-sectional shapes (aspect ratios of 1.3±0.2 across all groups), but differential cross-sectional areas (means±SD) that were notably smaller in male WT control aortas. Importantly, there was a marked reduction in collagen fibril density in male WT mice following BAPN. F, G. Results shown as probability distributions by sex. H. Across the 8 groups examined, burst pressure was found to correlate significantly with collagen fibril area fraction derived from transmission electron microscopy.